



HAL
open science

Impact of the transient formation of molecular hydrogen on the microcrack nucleation and evolution in H-implanted Si (001)

S. Personnic, K.K. Bourdelle, F. Letertre, A. Tauzin, Nikolay Cherkashin, Alain Claverie, R. Fortunier, H. Klocker

► To cite this version:

S. Personnic, K.K. Bourdelle, F. Letertre, A. Tauzin, Nikolay Cherkashin, et al.. Impact of the transient formation of molecular hydrogen on the microcrack nucleation and evolution in H-implanted Si (001). *Journal of Applied Physics*, 2008, 103 (2), pp.23508-1 - 23508-9. 10.1063/1.2829807 . hal-01736058

HAL Id: hal-01736058

<https://hal.science/hal-01736058v1>

Submitted on 23 Mar 2018

HAL is a multi-disciplinary open access archive for the deposit and dissemination of scientific research documents, whether they are published or not. The documents may come from teaching and research institutions in France or abroad, or from public or private research centers.

L'archive ouverte pluridisciplinaire **HAL**, est destinée au dépôt et à la diffusion de documents scientifiques de niveau recherche, publiés ou non, émanant des établissements d'enseignement et de recherche français ou étrangers, des laboratoires publics ou privés.

Impact of the transient formation of molecular hydrogen on the microcrack nucleation and evolution in H-implanted Si (001)

S. Personnic, K. K. Bourdelle, F. Letertre, A. Tauzin, N. Cherkashin, A. Claverie, R. Fortunier, and H. Klocker

Citation: *Journal of Applied Physics* **103**, 023508 (2008); doi: 10.1063/1.2829807

View online: <https://doi.org/10.1063/1.2829807>

View Table of Contents: <http://aip.scitation.org/toc/jap/103/2>

Published by the [American Institute of Physics](#)

Articles you may be interested in

[Development of microcracks in hydrogen-implanted silicon substrates](#)

Journal of Applied Physics **114**, 123513 (2013); 10.1063/1.4821239

[Investigation of the cut location in hydrogen implantation induced silicon surface layer exfoliation](#)

Journal of Applied Physics **89**, 5980 (2001); 10.1063/1.1353561

[Effect of the order of He⁺ and H⁺ ion co-implantation on damage generation and thermal evolution of complexes, platelets, and blisters in silicon](#)

Journal of Applied Physics **119**, 135308 (2016); 10.1063/1.4945032

[Study of the formation, evolution, and dissolution of interfacial defects in silicon wafer bonding](#)

Journal of Applied Physics **107**, 093513 (2010); 10.1063/1.3357389

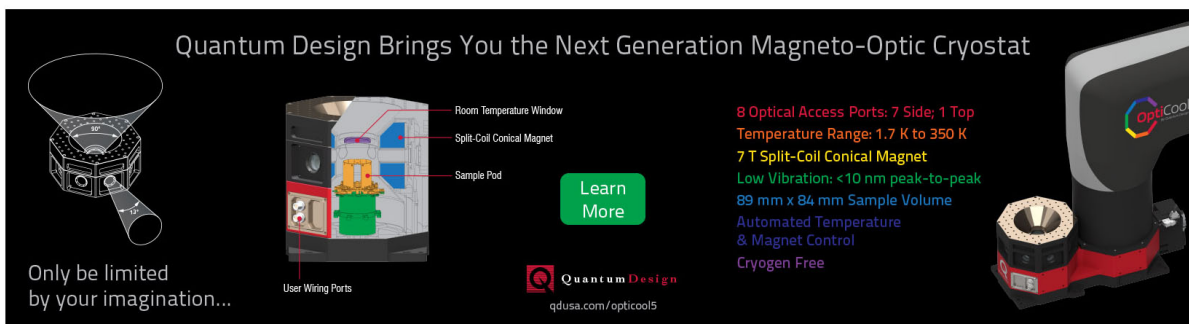
[Study of extended-defect formation in Ge and Si after H ion implantation](#)

Applied Physics Letters **86**, 181910 (2005); 10.1063/1.1906319

[Cracks and blisters formed close to a silicon wafer surface by He-H co-implantation at low energy](#)

Journal of Applied Physics **118**, 245301 (2015); 10.1063/1.4938108

Quantum Design Brings You the Next Generation Magneto-Optic Cryostat



Only be limited by your imagination...

Learn More

Quantum Design
qdusa.com/opticool5

8 Optical Access Ports: 7 Side; 1 Top
Temperature Range: 1.7 K to 350 K
7 T Split-Coil Conical Magnet
Low Vibration: <10 nm peak-to-peak
89 mm x 84 mm Sample Volume
Automated Temperature & Magnet Control
Cryogen Free

Impact of the transient formation of molecular hydrogen on the microcrack nucleation and evolution in H-implanted Si (001)

S. Personnic, K. K. Bourdelle,^{a)} and F. Letertre

Silicon-on-Insulator Technologies (SOITEC), Parc Technologique des Fontaines, 38926 Crolles Cedex, France

A. Tauzin

CEA-DRT-LETI, CEA-GRE, 17 Rue des Martyrs, 38054 Grenoble Cedex 9, France

N. Cherkashin and A. Claverie

CEMES/CNRS, nMat Group, BP 4347, F-31055 Toulouse, France

R. Fortunier and H. Klocker

EMSE, 158 Cours Fauriel, 42023 Saint-Etienne Cedex 2, France

(Received 17 September 2007; accepted 7 November 2007; published online 22 January 2008)

We study the implant-induced hydrogenated defects responsible for the Smart Cut™ layer transfer of Si (001) films. Different experimental methods are used to quantify the time dependence of the defect evolution and interactions during isothermal annealings. An optical characterization technique was developed for the statistical analysis of the formation and growth of micrometer size microcracks in the buried implanted layer. We show that the formation of molecular hydrogen is dominated by a transient phenomenon related to the rapid dissociation of the hydrogenated point defects. The impact of the H₂ formation kinetics on the microcrack evolution is described and the physical mechanisms involved in their growth are identified. A comprehensive picture of the fracture phenomenon in H implanted Si leading to the full layer transfer is proposed and discussed.

© 2008 American Institute of Physics. [DOI: [10.1063/1.2829807](https://doi.org/10.1063/1.2829807)]

I. INTRODUCTION

The discovery of the way to fabricate silicon-on-insulator (SOI) structures with the Smart Cut™ technology¹ has significantly enhanced the scope of applications of ion implantation. Hydrogen among other species is used to produce SOI wafers. It is well known that H is mobile and has a strong chemical activity in crystalline Si.² During H implantation a large variety of defects are created. For the room temperature implants the hydrogenated point defects (HPDs) are represented largely by the vacancy-hydrogen complexes. In addition, two-dimensional defects named platelets are formed in the implant-induced damage zone.³ It has been shown by transmission electron microscopy (TEM) that during thermal annealing these defects undergo an Oswald ripening process interchanging the H atoms they contain.⁴ The corresponding growth of the platelets induces the formation of large microcracks in the narrow depth region around project range of the H ions, R_p .⁵ The propagation and interaction of the microcracks lead to the full layer transfer of Si in the presence of a stiffener.^{1,5} Despite significant efforts, many physical aspects of the evolution of the hydrogenated defects from clusters to platelets then to microcracks are still unclear.

In this article, we present a time-dependence study of the hydrogenated defects responsible for the transfer of Si (001) thin layers during isothermal treatments. In the text we will distinguish the following.

- (i) HPDs, i.e., the multivacancies V_mH_n , the monovacancies

VH_n , and the H₂^{*} defects (Si–H_{AB} and Si–H_{BC}).

- (ii) Hydrogenated extended defects, HEDs, i.e., platelets and microcracks.

Different experimental methods are used to quantify defect evolution and interactions. An optical characterization technique has been developed for the statistical analysis of the buried microcracks. We show that the formation of hydrogen molecules during annealing is dominated by a transient phenomenon related to the rapid dissociation of the specific HPDs. The impact of the H₂ formation kinetics on the HEDs evolution is investigated and the physical mechanisms involved in their growth are identified. The presented results elucidate and quantify many aspects of the fracture phenomenon in H implanted Si (001).

II. EXPERIMENTS

200 mm *p*-type czochralski silicon (001) substrates were implanted with H at an energy of about 40 keV and a dose of a few 10¹⁶ cm⁻² through a 145 nm thick thermally grown oxide. After implantation and hydrophilic bonding to a base substrate, the structures were cut into sample pieces. These samples underwent annealing at temperatures between 350 and 500 °C for different times t_a ranging from 30 s to 51 h.

In a previous study⁶ we measured the time needed to obtain the full layer transfer at a given temperature: the splitting time $t_s(T)$. The data showed an Arrhenius-type dependence with an activation energy $E_a = 2.3 \pm 0.1$ eV. In this paper, in order to compare results obtained at different temperatures, the annealing time will be also expressed as fraction or percentage of $t_s(T)$.

^{a)}Electronic mail: konstantin.bourdelle@soitec.fr.

Different physical characterization techniques were used to track the behavior of implanted hydrogen and the evolution of the HPDs and HEDs during annealing. The H depth profiles were obtained by secondary ion mass spectroscopy (SIMS) technique using the MCs_2^+ method suitable for analysis of light electronegative elements.⁷ A Cameca IMS-5F apparatus with a 2 keV Cs^+ sputtering beam operated under a vacuum of $\sim 1 \times 10^{-9}$ Torr in the sample chamber. The elastic recoil detection analysis (ERDA) with a 2.3 MeV He analyzing beam was performed to monitor the total amount of H retained in the samples.

Fourier transform infrared spectroscopy (FTIR) was carried out in the multiple internal reflection mode with a Bruker IFS 55 spectrometer (resolution of 4 cm^{-1}) to quantify the types and relative distributions of hydrogenated defects in the as-implanted and annealed samples. Fitting of the FTIR spectra was performed using the GRAMS program.⁸ To deconvolute the spectra, we considered the well-known stretching modes for Si-H_n defects.^{2,9-11} Following the analysis in Ref. 2 we assumed that the absorption cross sections for the infrared light are the same for the different Si-H_n chemical bonds in the range of $1800\text{--}2250 \text{ cm}^{-1}$. The intensity of a given stretching mode is then directly proportional to the amount of hydrogen in the corresponding configuration. The peaks in the spectrum were fitted by a Gaussian-type profile with the width corresponding to the resolution of the spectrometer. For the quantitative analysis we have combined the peaks into several bands. That eliminates some uncertainties related to the assignment of certain Si-H_n modes.

The platelet populations were analyzed by cross sectional transmission electron microscopy (XTEM) mostly under out-of-Bragg strongly out-of-focus conditions, suitable for the Fresnel imaging of these phase objects. A JEOL 2010 electron microscope operating at 200 keV was used. The XTEM characterization was restricted to the samples annealed for the times shorter than 50% of $t_s(T)$. For longer annealings, the samples become very fragile and cannot be prepared using standard techniques. With more complicated preparation procedures involving the encapsulation of the overall structure and sample thinning by focused ion beam, large microcracks, up to $1\text{--}2 \mu\text{m}$ in diameter, have also been observed.⁵ The statistical analysis of these defects by XTEM is, however, not possible.

To image the buried microcracks we used a Wyko NT 3300 optical profiler in a phase shifting interferometry mode with a white-light beam filtered at 632 nm. The sample preparation for this analysis was as follows. After H implantation, a SiO_2 film was deposited onto the wafers using the plasma enhanced chemical vapor deposition technique. The deposition temperature was kept below $200 \text{ }^\circ\text{C}$ in order to avoid H redistribution. For deposited thickness larger than $10 \mu\text{m}$ the SiO_2 stiffener completely prevented formation of blisters at the Si surface during annealing, leading to a full layer transfer. The corresponding $t_s(T)$ was exactly the same as for the bonded SOI structure with a Si wafer as a stiffener. Atomic force microscopy showed no difference in postsplit surface roughness between bonded SOI and the structure with deposited SiO_2 layer as a stiffener. Due to transparency

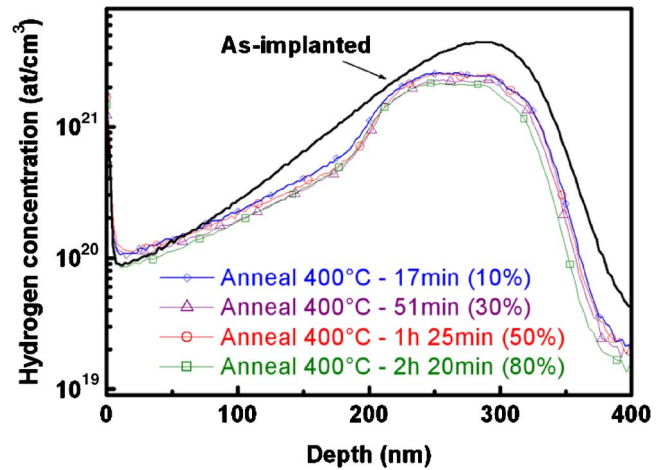


FIG. 1. (Color online) Hydrogen SIMS profiles before and after isothermal annealings at $400 \text{ }^\circ\text{C}$.

of the SiO_2 film at the wavelength of 632 nm and relatively small absorption in Si the observation of buried microcracks is possible. The beam of the profiler can be focused either at the depth region where the microcracks develop or at the surface of the SiO_2 stiffener. The microcracks with a size larger than $1 \mu\text{m}$ can be imaged using this technique. Laser marking of the sample surface allows observation of the evolution of the same population of the microcracks.

Some companion samples were annealed without any oxide layer on the Si surface to induce the formation of blisters. For such samples, the optical profiler was used to measure the diameter and height of the blisters. The corresponding volume and amount of the molecular hydrogen contained in the blisters was estimated based on the approach developed in Refs. [12,13].

III. RESULTS AND INTERPRETATION

A. Time dependence of molecular H_2 formation

Figure 1 shows the evolution of the H depth distribution during annealing. Two main features are observed. First, there is a “transient” signature: changes in the depth profile occur only during initial stage of the anneal, i.e., for $t_a < t_s(T)/10$. The redistribution shows the evidence of an “up-hill diffusion:” the concentration gradients at the slopes of the profile increase after annealing while a plateau is observed in the R_p region. These are classical features observed when the precipitation of a second phase from a supersaturated matrix occurs since the precipitates tend to absorb the free mobile species around them. Second, in agreement with our previous report,⁶ we note an apparent H “dose loss”: reduction in the integrated area under the profile after annealing. That is not consistent with the small redistribution of H in the surface region and might be due to H precipitation in a form that is not or only partially detected by SIMS.

To verify this assumption we have undertaken additional experiments with the ERDA technique sensitive to the total hydrogen content in the sample regardless of the chemical state. The normalized amounts of H determined by SIMS and ERDA are plotted in Fig. 2 as a function of percentage of $t_s(T)$ for two temperatures. It is seen that the amount of hy-

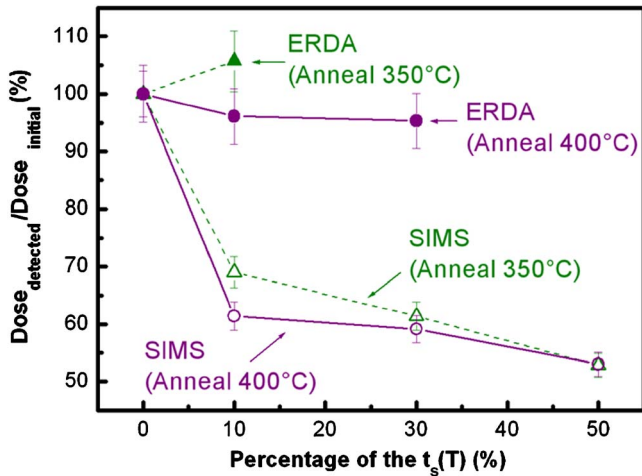


FIG. 2. (Color online) Normalized hydrogen dose measured by SIMS and ERDA as a function of percentage of $t_s(T)$ for isothermal annealings at 350 and 400 °C.

drogen detected by SIMS strongly decreases during the first stage of annealing, whereas the ERDA signal does not change significantly with time. This is a clear confirmation that the decrease of the SIMS signal seen in Fig. 1 is not due to the outdiffusion of H from the implanted region but to some rearrangement of the H atoms in a form not detectable by SIMS.

Figure 3 shows that the fast rearrangement of the hydrogenated defects measured by FTIR also occurs during the initial stage of annealing. The variation of the integrated intensity of the FTIR signal along with the normalized dose obtained by SIMS is depicted in Fig. 4 as a function of the percentage of $t_s(T)$. A similar transient behavior is observed, although the amplitude drop is more pronounced for the FTIR signal.

Using the deconvolution procedure described in Sec. II the time evolution of the different types of hydrogenated defects was extracted. The normalized intensity values (annealed at 450 °C) are shown in Fig. 5 for: (a) the multivacancy defects V_mH_n (broadband between 1880 and 2025 cm^{-1}); (b) the monovacancy defects $VH_{3,4}$ (band be-

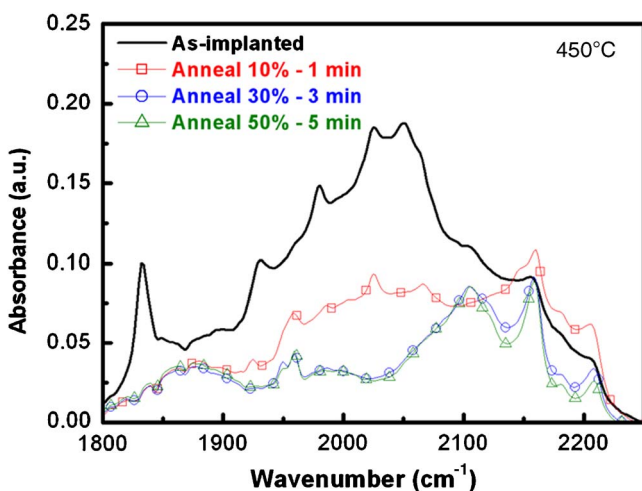


FIG. 3. (Color online) FTIR spectra of the Si-H stretching modes in H implanted Si before and after isothermal annealings at 450 °C.

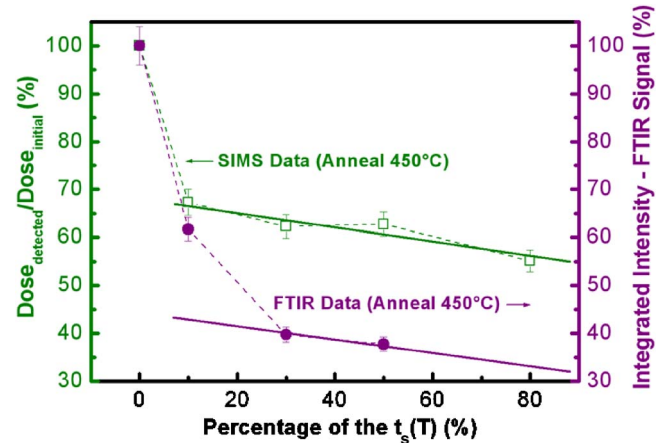


FIG. 4. (Color online) Normalized SIMS dose and integrated intensity of FTIR spectra as a function of percentage of $t_s(T)$ for isothermal annealings at 450 °C.

tween 2160 and 2210 cm^{-1}); (c) the H_2^* defects (modes at 1832 and 2052 cm^{-1}); (d) VH_2 defects and the H passivating the internal (100) surfaces (modes between 2085 and 2130 cm^{-1}). Two very different types of behavior are observed. On one hand [Figs. 5(a) and 5(c)], the concentrations of multivacancies and H_2^* defects rapidly decrease during the first 30% of $t_s(T)$. There is little change in concentration of these defects for longer annealing times. On the other hand, Fig. 5(b) indicates that only a small fraction of the initially predominant V_mH_n defects, $\sim 3\%$ of the implanted H-dose, might be converted into $VH_{3,4}$ defects during the initial stage of annealing. The details of the evolution of the intensity of the modes related to $VH_{3,4}$ defects will be discussed in Sec. III B together with the XTEM data.

The decrease of the infrared band around 2100 cm^{-1} during transient stage may be associated with the dissociation of the VH_2 defects. The corresponding stretching mode is in the same wave number range, i.e., around 2121 cm^{-1} .⁹ Myers *et al.*¹⁴ found that the binding energy of hydrogen with vacancies is smaller than that for hydrogen passivating the internal surfaces. Therefore the dissolution of VH_2 defects is energetically favorable in agreement with the information obtained from the deconvolution of the infrared spectra [Fig. 5(d)].

Theoretical calculations¹⁵ indicate that H_2 can be stable at the tetrahedral interstitial T_d sites. Other reports demonstrated that the existence of point defects in Si promotes the dissociation of H_2 ,¹⁶ with a dissociation rate increasing with the degree of the crystalline disorder.¹⁷ Our FTIR data show that during annealing the morphology of the implant damage changes, notably during the initial stage of the annealing, leading to an overall strong decrease of the HPD concentration. We cannot rule out that this transformation can produce molecular H_2 stable at the T_d sites. The solubility of H_2 in Si at room temperature is, however, negligibly small.² The concentration of H_2 located on the T_d sites must be, therefore, very low.

The combination of SIMS, ERDA, and FTIR data can be explained by the rapid conversion of hydrogen trapped within HPDs in the as-implanted state into molecular H_2 .²

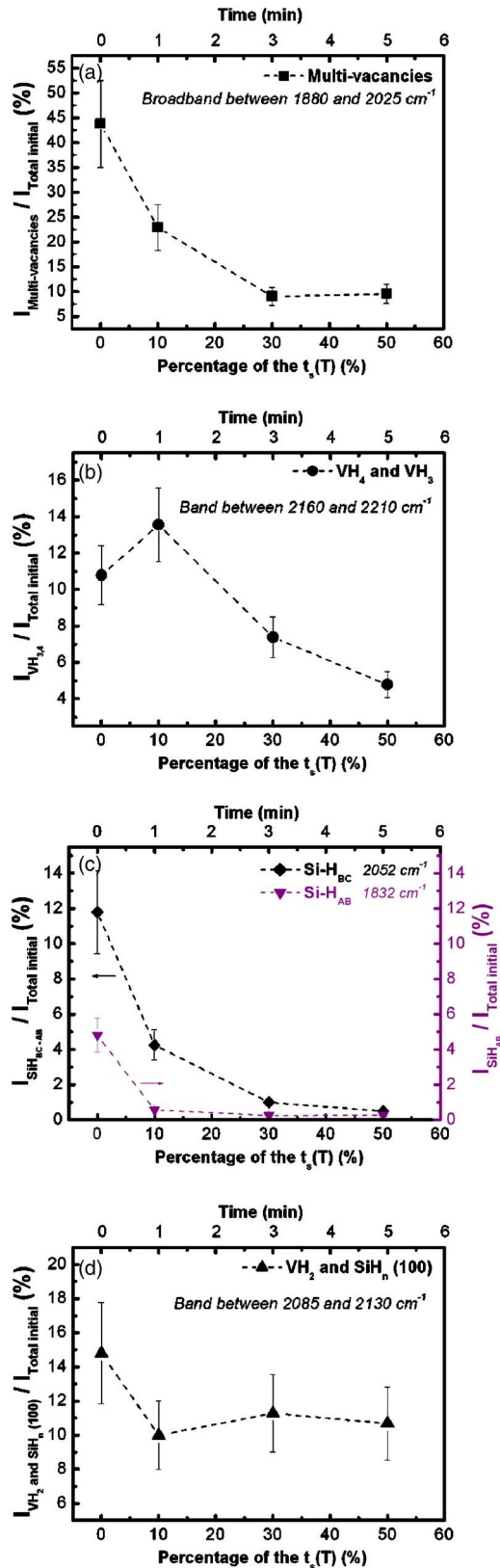


FIG. 5. (Color online) Evolution of the multivacancy (a), monovacancy (b), H_2^* (c), and H passivating (100) internal surfaces (d) FTIR modes during annealing at 450 °C.

We believe that the observed SIMS dose loss is due to the limited capability of this technique to detect molecular H_2 . The transient time domain during which the dissociation/recombination of the multivacancies and H_2^* defects takes

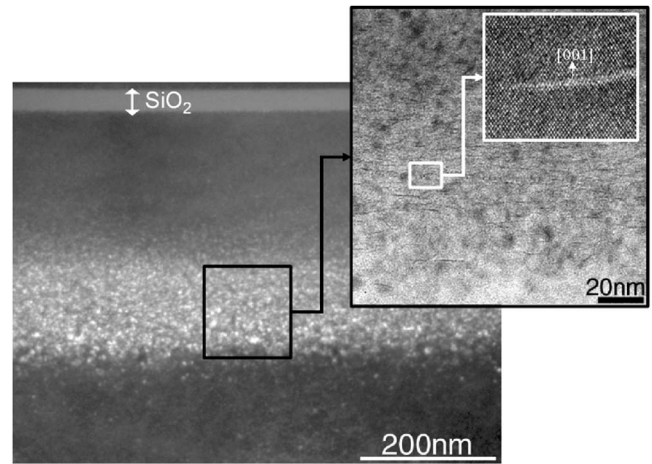


FIG. 6. TEM micrographs of the damage zone (a), platelets population (b), and (001) platelet parallel to the wafer surface (c).

place can be directly related to the precipitation of hydrogen in molecular form. In our opinion, the high pressure of H_2 within the HEDs (Ref. 4) as well as the high ionization cross section for H_2 limits the capability of the SIMS technique to detect hydrogen trapped in these defects. During advancement of the sputtering crater in the condition of high vacuum the pressurized gaseous H_2 quickly leaves the area of ionization drastically decreasing the SIMS yield.

It is rather difficult to determine the amount of molecular hydrogen in the as-implanted state. With our data, however, it is possible to quantify the amount of molecular H_2 after the end of the transient stage. From the reduction of the SIMS signal, and FTIR data we can deduce that the HEDs contain more than 70% of the molecular H_2 created during the thermal treatment. A smaller fraction of H_2 molecules, less than 30%, corresponding to the difference between SIMS and FTIR signals might be trapped into small clusters such as the stable V_mH_n defects and, in minor proportion, is located in the T_d sites of the Si matrix.

Analysis of the integrated intensity of the FTIR spectra shows that the amount of molecular hydrogen formed after long annealing, 80% of $t_s(T)$, corresponds to $\sim 60\% - 65\%$ of the implanted dose. We assume here that H not detected by FTIR in the form of SiH_n defects is in molecular form since ERDA shows negligible outdiffusion of H from the implanted region. Figure 5(a) indicates that a fraction of V_mH_n defects, corresponding to about 10% of the implanted dose, remains stable upon this long time annealing. We believe that a number of H_2 molecules might be trapped within the clusters created by the more stable V_mH_n defects. The existence of such configuration has been observed in the other reports.¹⁸⁻²⁰

B. Platelets nucleation and growth: XTEM analysis

XTEM was used to quantitatively follow the evolution of the characteristics of the populations of platelets during annealing of the same set of samples. A typical damage zone was observed between 170 and 370 nm below Si surface and the fracture plane was at a depth of about 300 nm [Fig. 6(a)]. Two families of platelets were found with habit planes either

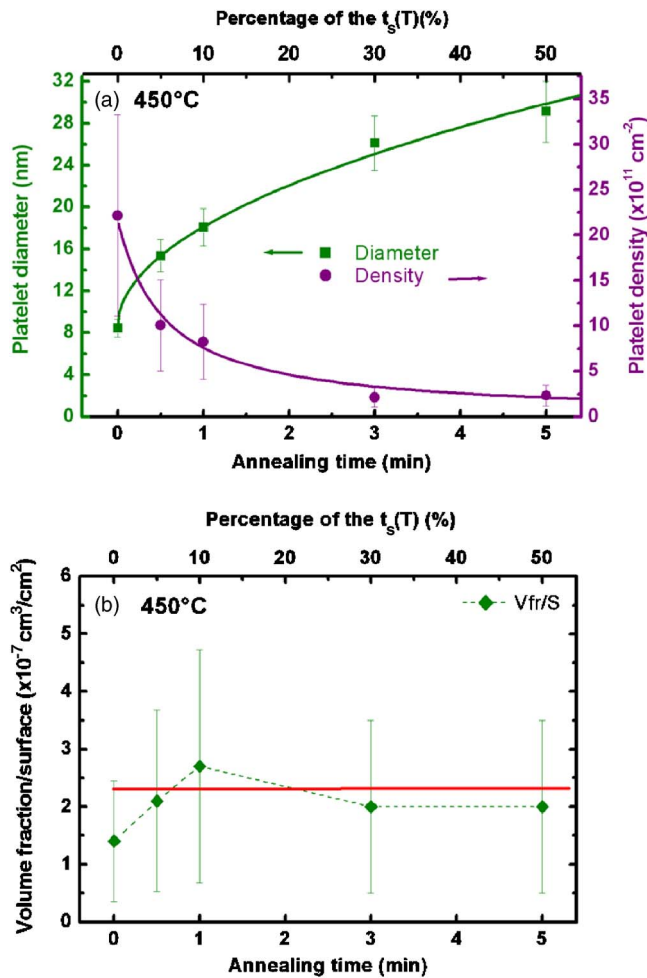


FIG. 7. (Color online) Evolution of mean diameter and surface density (a) and platelet volume fraction per unit area (b) as a function of the annealing time at 450 °C.

lying on the (001) plane parallel to the wafer surface [Figs. 6(b) and 6(c)] or on two sets of (111) plane. Under our experimental conditions, the (111) platelets are located deeper in the damage zone and are detected in considerably smaller densities than the (001) platelets. Using the method described in details in Ref. 4, we have carried out a statistical analysis of the characteristics of the platelet populations found after each annealing step. Figure 7(a) presents the time evolution of the mean size and the density of the (001) platelets during annealing at 450 °C. From these results, the surface and the volume fractions the platelet population can be extracted [Fig. 7(b)].

It is striking to note that this surface fraction increases again during the first stage of the annealing. Since the density of platelets does not increase in the mean time, the nucleation stage of the platelets is already completed after implantation. During the transient stage, for $t_a < 10\%$ of $t_s(T)$, the platelets are involved in a “pure growth” regime during which the existing nuclei grow by “pumping” H from other less stable defects in the matrix, invisible by TEM. This is consistent with the FTIR and SIMS results showing a dramatic drop of the integrated signal intensities also during the same transient stage. Only the IR band corresponding to the monovacancies defects $VH_{3,4}$ increases in amplitude dur-

ing this period of time [Fig. 5(b)]. Since these $VH_{3,4}$ defects are thought to be the precursors of the platelets,^{2,21} our IR data show that only 3% of the implanted dose is used for formation of new platelets during the transient stage of annealing.

The combination of FTIR, SIMS, and TEM results leads to the following scenario for the platelets growth. The H_2 molecules are produced mostly following the dissociation of HPDs and the migration of H toward the platelets during the transient period. As the platelets grow by the injection of H from other less stable defects, the pressure inside them quickly increases leading to their propagation. Later on, for $t_a > 10\%$ of $t_s(T)$, the average diameter of the platelets still increases and their density decreases in such a manner that the surface and volume fractions per unit area they occupy remain nearly constant. These characteristics are typical of a conservative Ostwald ripening mechanism⁴ during which the platelets interchange the species they are composed of, namely, hydrogen atoms and vacancies. This scenario is consistent with the FTIR observations where the intensity of the stretching modes around 2100 cm^{-1} assigned to H passivating the internal (100) surfaces of the platelets remains constant during the same period of time [Fig. 5(d)].

C. Microcrack evolution

The characterization of annealed samples by XTEM is restricted to times shorter than 50% of $t_s(T)$ for which the maximum platelet diameter is of about 40 nm. The optical characterization of the microcrack evolution at $\sim 300 \text{ nm}$ below the Si surface was therefore performed using phase shifting interferometry technique described in Sec. II.

Figure 8(a) shows a typical image of the buried microcracks obtained after annealing of the implanted wafers covered by a thick SiO_2 layer, for t_a corresponding to 40% of $t_s(T)$. Clearly, this technique evidences the presence of a population of microcracks with sizes ranging from a few to several micrometers and with a density of the order of 10^6 cm^{-2} . No blisters are observed for such conditions as confirmed by imaging of the wafer surface [Fig. 8(b)]. Figure 9 shows the isothermal evolution of the microcracks at 350 °C. Two distinct phenomena are observed. First, the smallest microcracks dissolve (circles in Fig. 9), while the largest grow. This behavior suggests that microcracks are also involved in Ostwald ripening, i.e., interchange the vacancies and hydrogen atoms they are composed of. The growth of the largest microcracks, however, occurs also, in part, through the coalescence between neighboring, already large, microcracks (squares in Fig. 9). This phenomenon does not involve the motion of these defects but instead appears as the result of the sudden overlapping of their strain fields as they grow by the regular Ostwald ripening mechanism. Such a geometric coalescence leads to the random formation of large microcracks with the size up to tens of micrometers after annealing for 50% of $t_s(T)$.

This growth mechanism gives rise to the formation of microcracks of irregular shapes, in contrast with the circular shape of the platelets. We have performed a statistical analysis of such images, measuring the surface area occupied by

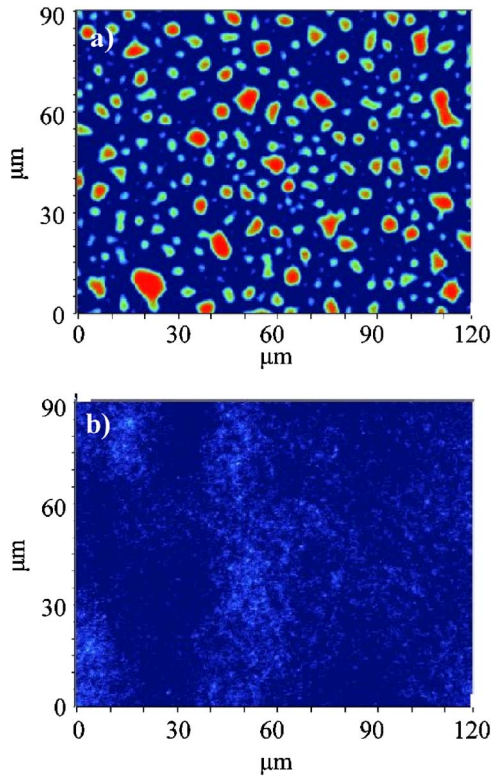


FIG. 8. (Color online) Optical profiler images obtained for the wafer with a thick stiffener after annealing at 400 °C: buried microcracks (a) and the surface of the deposited SiO₂ layer (b).

the microcracks and assigning them the mean diameter they would have if circular in shape. Figure 10 depicts the size distributions of the microcracks for different isothermal annealings at 400 °C. It is striking to note that, for $t_a \geq 50\%$ of $t_s(T)$, the distribution becomes bimodal. The amplitude of the first peak decreases during annealing while the relative contribution of the second increases. The position of the first peak only slightly shifts toward larger diameters during the first stage of annealing. That indicates that the contribution of the Ostwald ripening mechanism to the overall growth of the microcracks is marginal. Alternatively, the relative increase of the second peak, centered at the size slightly larger than twice that of the first peak, is the signature of the coalescence process.

The important conclusions from this analysis are that microcrack coalescence occurs during their “regular” growth by Ostwald ripening and that this coalescence process is almost conservative. These first findings are confirmed by the

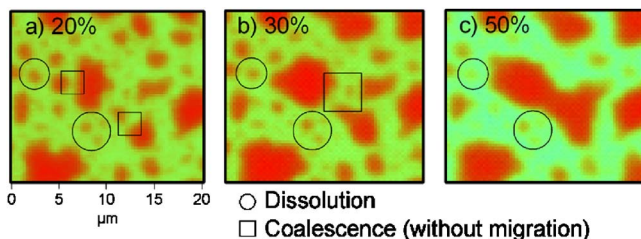


FIG. 9. (Color online) Optical profiler images of buried microcracks after an annealing at 350 °C for 20% (a), 30% (b), and 50% (c) of $t_s(T)$. The images illustrate the Ostwald ripening and the coalescence mechanisms.

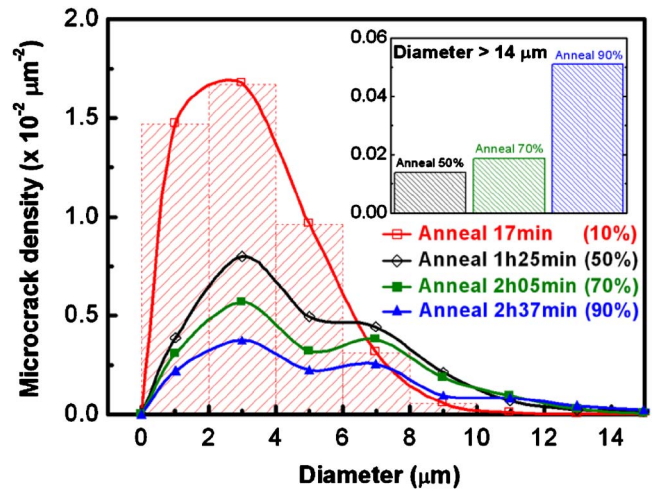


FIG. 10. (Color online) Size distributions of the microcracks after different annealings at 400 °C.

quantitative analysis of the data shown in Fig. 11. For annealing times ranging from 10% to 80%–90% of $t_s(T)$, the mean diameter and the inverse of the density of microcrack population show a linear dependence on the square root of the time and on the time, respectively [Figs. 11(a) and 11(b)]. This time dependence is characteristic of the Ostwald ripening for two-dimensional precipitates. During the same time interval the surface fraction covered by these defects remains constant, at about 30% of the total surface of the wafer [Fig. 11(c)]. The increase seen at the beginning of the annealing, from 10% to 20% of $t_s(T)$, might be due to the growth of some microcracks which sizes were below the detection limit, i.e., 1 μm. We cannot rule out also the spontaneous formation (nucleation) of new microcracks.

D. Driving force behind microcrack growth

Using the SIMS technique we have shown previously⁶ that the kinetics of H₂ formation in HEDs is close to that for the layer transfer. It has been suggested by Freund²² that the growth of an individual microcrack is driven by the pressure of the hydrogen gas. In order to verify whether the quantitative analysis presented in Secs. III B and III C is consistent with this assumption, we simulated the dependence of the individual microcrack radius on the annealing time at 400 °C.

The microcracks growth by the Ostwald ripening mechanism implies that the pressure of H₂ within the larger ones increases due to the arrival of hydrogen from the smaller ones. When the magnitude of the gas pressure exceeds the critical value P_c the microcrack propagation occurs. The increase of the microcrack diameter can be modeled based on Griffith's criterion.²² From a simple energy balance calculation, the P_c value can be obtained as a function of the silicon properties and the microcrack radius.

Assuming a uniform pressure of H₂ molecules within the defect, Griffith's criterion can be formulated as follows:

$$\frac{d}{dR} \left(-\frac{4\pi(1-2\nu)P^2R^3}{3E} + 2\pi\gamma_{\text{Si}}R^2 \right) < 0, \quad (1)$$

where E is Young's modulus of silicon, γ_{Si} is the surface energy density, ν is the Poisson ratio, R is the radius of the microcrack, and P is the pressure of H_2 molecules. This equation gives the conditions for the microcrack propagation. The first part corresponds to the mechanical energy of a microcrack, and the second to the energy of the additional fracture surface.

The pressure can be estimated using the ideal gas law since the volume formed by the H_2 molecules is significantly smaller than that for the microcrack,

$$P = \frac{N_{\text{H}_2}kT}{\pi R^2 h}, \quad (2)$$

where h is the microcrack thickness, k is Boltzman's constant, and N_{H_2} the number of hydrogen molecules in the microcrack.

To use Griffith's criterion we need to estimate the number of H_2 molecules within an individual microcrack. The amount of molecular hydrogen within the HEDs in the damage zone can be obtained, e.g., with the SIMS technique. To estimate the amount of H_2 contained in the microcracks located in the immediate vicinity of R_p , we have used a different approximation. This value was obtained from the complementary blistering study (see Sec. II for experimental details). The results of statistical analysis (not shown here) indicate that the amount of H_2 in the blisters corresponds to about 60% of the molecular hydrogen obtained by SIMS technique for the bonded samples.

For the initial condition, i.e., the as-implanted state, the microcrack embryo is approximated by a platelet of 10 nm in diameter and 1 nm in thickness [see Fig. 7(a) and Ref. 5]. To simulate the growth of a larger (radius $> 1 \mu\text{m}$) microcrack from a platelet during the initial stage of annealing the following assumptions have been made: (1) there are no H_2 molecules in the platelet in the as-implanted state; (2) the number of the H_2 molecules in the microcrack after annealing for $t_a = 10\%$ of $t_s(T)$ was obtained using the experimental density of the microcracks [see Fig. 11(b)]; (3) based on the XTEM observation the defect thickness was assumed to "increase" from 1 to 2 nm. Figure 12 shows that the calculated radius of a microcrack is in a good agreement with the experimental value for the average radius of the population for 10% of $t_s(T)$.

The same approach was used to fit the experimental data points for $t_a > 10\%$ of $t_s(T)$. The only fitting parameter was the microcrack thickness varied from 2 to 6 nm as a linear function of the annealing time. Figure 12 shows a good agreement between experiments and simulations for t_a up to 80% of $t_s(T)$. For longer time there are small deviations between the model and the experiments. The range of the microcrack thickness used to fit the experimental data was the same for all temperatures studied in this paper.

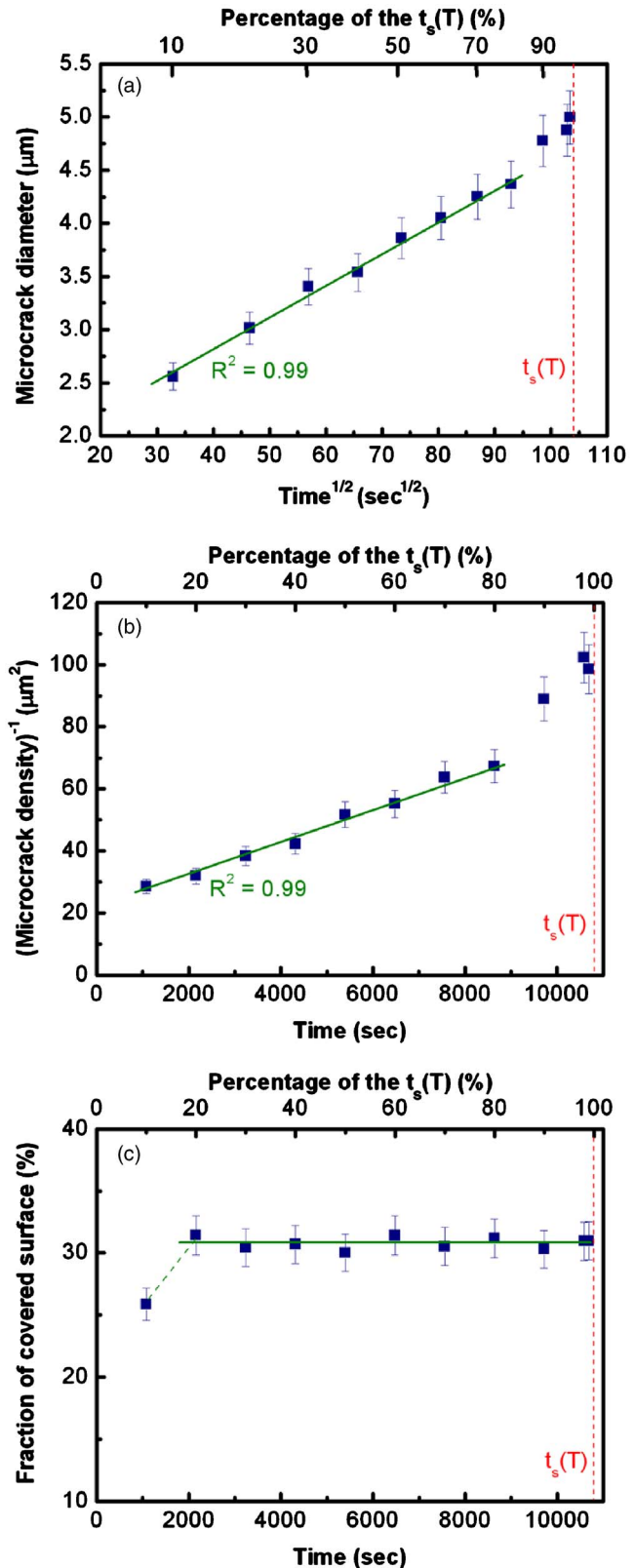


FIG. 11. (Color online) Dependence of the mean diameter of the microcrack population on the square root of the annealing time (a) at 400°C . Corresponding time dependences of the inverse surface density (b) and fraction of covered surface (c).

IV. DISCUSSION

The presented results support the following scenario of the fracture phenomenon in H implanted (001) Si. In the

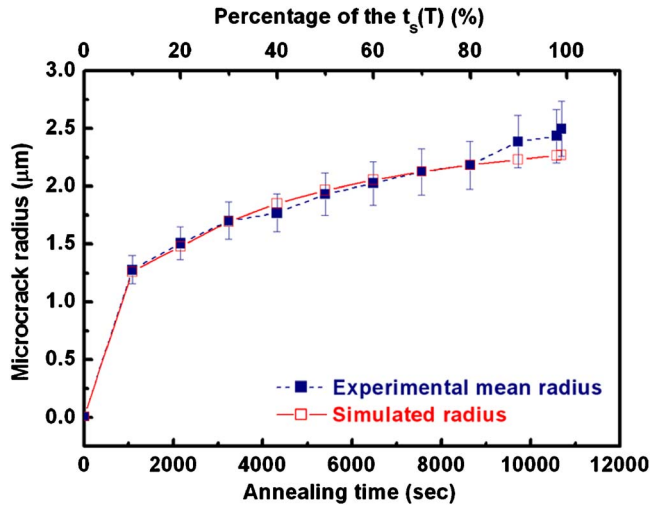


FIG. 12. (Color online) Time dependence of the microcrack radius for annealings at 400 °C: experimental data for the average size of the population and simulation results for the individual microcracks based on Griffith criterion.

as-implanted state, the damage zone is composed of numerous HPDs and platelets. The majority of platelets are on (001) plane parallel to the wafer surface. During the first period of the isothermal annealing a fast dissolution of the unstable HPDs takes place. The dominating precipitation phenomenon is characterized by the three simultaneous mechanisms.

- (i) The growth of platelet by a crack propagation mechanism induced by the fast arrival of molecular H_2 .
- (ii) The random nucleation of platelets, which is not entirely completed during the ion implantation.
- (iii) Ostwald ripening for the platelet population in the damage zone.

After the end of the transient stage, i.e., $t_a \sim t_s(T)/10$, buried microcracks, with the size $>1 \mu\text{m}$, are detected. We believe that a microcrack forms as a result of the coalescence of numerous platelets. These “precursor” platelets have been nucleated and grown in close proximity and at about the same depth: around R_p . The platelets predominantly grow by crack propagation mechanism due to H_2 injection at the beginning of annealing. They mechanically interact and this catastrophic interaction gives rise to the formation of an individual microcrack. This is not a common event as it can be judged from the respective densities of platelets and microcracks. There are about 1×10^6 less microcracks than platelets in the Si matrix during annealing. We can assume that the probability to form these large microcracks at the beginning of the annealing increases with the initial platelet density and thus with the implanted dose. These conditions are better met in the region close to R_p where the density of platelets and H_2 is higher and lead to the preferential formation of microcracks at that depth. For this reason, the microcracks have very narrow depth distribution as compared to those for platelets. As a consequence, two populations of HEDs coexist in the damage zone after initial stage of annealing: platelets with a mean diameter of 20 nm and microcracks with an average size of 2.5 μm .

XTEM analysis shows that for $t_a > t_s(T)/10$ the platelets within the damage zone grow via conservative Ostwald ripening mechanism. The microcracks growth for t_a between 10% and 80% of $t_s(T)$ is governed by a complex process involving different phenomena: an Ostwald ripening mechanism is coupled with a crack propagation process. The dissolution of the smaller microcracks leads to the continuous formation of H_2 molecules within the bigger ones. The more developed microcracks grow by a crack propagation mechanism due to the high hydrogen gas pressure. In a good agreement with our model described in Sec. III D and our previous results⁶ the driving force behind the layer transfer is the formation of H_2 in HEDs. The propagation mechanism of the individual microcracks leads to a random coalescence process between neighboring larger microcracks. We have shown in Sec. III C that this phenomenon occurs as the result of the sudden overlapping of their strain fields.

The strong impact of the coalescence on the statistical parameters of the microcrack population becomes evident at the end of the thermal treatment for $t_a > 80\% - 90\%$ of $t_s(T)$ when a growth mode changes. At this stage a strong direct interaction between the HEDs leads to an “accelerated” growth of the microcracks manifesting itself through the fast decrease of their density and the rapid increase of their mean size. The coalescence process due to the rupture of the Si lattice becomes predominant, leading to the full layer transfer. A model based on the Griffith criterion cannot describe the increase of the mean radius related to this mechanism since it does not take into account direct interactions between microcracks. A more sophisticated model describing the microcrack interaction during the catastrophic process occurring at the later stages of annealing (Fig. 12) has to be developed.

V. SUMMARY

The evolution of the H implant-induced defects in Si during isothermal annealings has been studied. The transient phenomenon during the initial stages of annealing is characterized by the fast dissolution of HPDs with about 60% of the implanted hydrogen involved. The predominant chemical reaction during this process corresponds to the formation of molecular hydrogen. The molecular H_2 formation is not a linear function of the annealing time and has two regimes: a “fast-rate” domain due to dissociation of the hydrogenated complexes and a “slow-rate” domain occurring during remaining part of the thermal treatment.

Growth kinetics of HEDs can be divided into three stages. During the first 10% of the splitting time, the transient process of H_2 formation induces the development of two distinct HED populations: platelet-type defects and microcracks of several microns in diameter. The fracture plane therefore is already defined during the first stage of annealing. For longer annealings, between 10% and 80% of the $t_s(T)$, the smaller HEDs, platelet grow via an Ostwald ripening mechanism. For larger HEDs, microcracks, the growth mechanism is more complex involving besides Ostwald ripening the crack propagation and coalescence. It is driven by the continuous H_2 formation. In the last stage of annealing,

the larger microcracks under high hydrogen gas pressure have strong mechanical interactions by the sudden overlapping of their strain fields leading to a predominant geometric coalescence process. This “catastrophic” mechanism results in the full layer transfer of Si.

ACKNOWLEDGMENTS

F. Laugier is acknowledged for SIMS analysis and N. Rochat for the help with the infrared spectroscopy measurements.

¹M. Bruel, *Electron. Lett.* **31**, 1201 (1995).

²M. K. Weldon, V. E. Marsico, Y. J. Chabal, A. Agarwal, D. J. Eaglesham, J. Sapjeta, W. L. Brown, D. C. Jacobson, Y. Caudano, S. B. Christman, and E. E. Chaban, *J. Vac. Sci. Technol. B* **15**, 1065 (1997).

³N. M. Johnson, F. A. Ponce, R. A. Street, and R. J. Nemanich, *Phys. Rev. B* **35**, 4166 (1987).

⁴J. Grisolia, G. Ben Assayag, A. Claverie, B. Aspar, C. Lagahe, and L. Laanab, *Appl. Phys. Lett.* **76**, 852 (2000).

⁵B. Aspar, H. Moriceau, E. Jalaguier, C. Lagahe, A. Soubie, B. Biasse, A. M. Papon, A. Claverie, J. Grisolia, G. Benassayag, F. Leterte, O. Rayssac, T. Barge, C. Maleville, and B. Ghyselen, *J. Electron. Mater.* **30**, 834 (2001).

⁶S. Personnic, A. Tauzin, K. K. Bourdelle, F. Leterte, N. Kernevez, F. Laugier, N. Cherkashin, A. Claverie, and R. Fortunier, *AIP Conf. Proc.*

866, 65 (2006).

⁷P. Holliger, F. Laugier, and J. C. Dupuy, *Surf. Interface Anal.* **34**, 472 (2002).

⁸GRAMS software, <http://www.thermo.com/com/CDA/>.

⁹B. Bech Nielsen, L. Hoffmann, M. Budde, R. Jones, J. Goss, and S. Öberg, *Mater. Sci. Forum* **196–201**, 933 (1995).

¹⁰M. Shinohara, T. Kuwano, Y. Akama, Y. Kimura, and M. Niwano, *J. Vac. Sci. Technol. A* **21**, 25 (2003).

¹¹M. Suezawa, *Jpn. J. Appl. Phys., Part 2* **37**, L806 (1998).

¹²S. P. Timoshenko, *Resistance Des Matériaux*, Tome II (Dunod, Paris, 1981).

¹³C. M. Varma, *Appl. Phys. Lett.* **71**, 3519 (1997).

¹⁴S. M. Myers, D. M. Follstaedt, H. J. Stein, and W. R. Wampler, *Phys. Rev. B* **47**, 13380 (1993).

¹⁵P. Deak, L. C. Snyder, and J. W. Corbett, *Phys. Rev. B* **37**, 6887 (1988).

¹⁶S. K. Estreicher, J. L. Hastings, and P. A. Fedders, *Phys. Rev. B* **57**, R12 663 (1998).

¹⁷M. Kitajima, K. Ishioka, and S. Tateishi, *Mater. Sci. Eng., B* **58**, 13 (1999).

¹⁸K. Ishioka, M. Kitajima, S. Tateishi, K. Nakanoya, N. Fukata, T. Mori, K. Murakami, and S. Hishita, *Phys. Rev. B* **60**, 10852 (1999).

¹⁹T. Mori, K. Otsuka, N. Umehara, K. Ishioka, M. Kitajima, S. Hishita, and K. Murakami, *Physica B* **308–310**, 171 (2001).

²⁰W. Dünge, R. Job, Y. Ma, Y. L. Huang, T. Mueller, W. R. Fahrner, L. O. Keller, J. T. Horstmann, and H. Fieldler, *J. Appl. Phys.* **100**, 034911 (2006).

²¹F. A. Reboredo, M. Ferconi, and S. T. Pantelides, *Phys. Rev. Lett.* **82**, 4870 (1999).

²²L. B. Freund, *Appl. Phys. Lett.* **70**, 3519 (1997).